



ORIGINAL ARTICLE

Fabrication of ternary dual Z-Scheme AgI/ ZnIn₂S₄/BiVO₄ heterojunction photocatalyst with enhanced photocatalytic degradation of tetracycline under visible light



Shuhang Wang^{a,1}, Li Zhao^{a,1}, Luning Gao^b, Daiqiong Yang^b, Sijie Wen^b,
Wei Huang^{a,c}, Zexin Sun^d, Jifeng Guo^d, Xia Jiang^a, Changyu Lu^{b,d,*}

^a National Engineering Laboratory for Lake Pollution Control and Ecological Restoration, Chinese Research Academy of Environmental Sciences, Beijing 100012, PR China

^b Hebei Province Key Laboratory of Sustained Utilization & Development of Water Recourse, Hebei Province Collaborative Innovation Center for Sustainable Utilization of Water Resources and Optimization of Industrial Structure, Department of Water Resource and Environment, Hebei Geo University, No. 136 Huai'an Road, Shijiazhuang 050031, Hebei, PR China

^c State Environmental Protection Engineering Center for Pollution Treatment and Control in Textile Industry, College of Environmental Science and Engineering, Donghua University, Shanghai 201620, PR China

^d School of Water and Environment, Key Laboratory of Subsurface Hydrology and Ecology in Arid Areas, Ministry of Education, Chang'an University, No. 126 Yanta Road, Xi'an 710054, Shaanxi, PR China

Received 27 July 2021; accepted 27 July 2022
Available online 01 August 2022

KEYWORDS

Photocatalysis;
AgI/ZnIn₂S₄/BiVO₄;
Dual Z-
Scheme heterojunction;
Tetracycline

Abstract In this study, a novel ternary AgI/ZnIn₂S₄/BiVO₄(AZB) composite photocatalyst was successfully prepared by hydrothermal method and in-situ precipitation method. The as-synthesized samples were characterized by XRD, SEM, TEM, XPS and so on, and the photocatalytic activity was evaluated through photocatalytic degradation of tetracycline (TC) under visible light irradiation. When the molar ratio of Bi to Ag was 1:1, the degradation rate of TC can reach 91.44 % within 150 min. The AZB heterojunction demonstrated outstanding efficiency with the apparent reaction rate constants of 0.02118 min⁻¹ for TC removal, was 4.68, 3.27 and 3.27 times higher than that of pure BiVO₄, AgI and ZnIn₂S₄. Based on active species trapping experiments

* Corresponding author.

E-mail address: pzpzlxl@163.com (C. Lu).

¹ These authors contribute equally to this work.

Peer review under responsibility of King Saud University.



and ESR analysis, a dual Z-Scheme pathways among BiVO₄, AgI and ZnIn₂S₄ for effective separation of photogenerated charges was recommended. This work provided a promising insight for the design of ternary dual Z-scheme heterojunction with multilevel electron transfer to present greater photo-absorption, charge separation, and photodegradation for environmental decontamination.

© 2022 The Author(s). Published by Elsevier B.V. on behalf of King Saud University. This is an open access article under the CC BY-NC-ND license (<http://creativecommons.org/licenses/by-nc-nd/4.0/>).

1. Introduction

With economic development in recent years, environmental pollution, especially antibiotic pollution, have become increasingly serious (Li et al., 2022a; Lu et al., 2022a). Confronted with the difficult degradation of various antibiotic contaminant, photocatalytic oxidation with semiconductor have attracted considerable attention due to their low toxicity, high stability and environmental-friendly (Zhang et al., 2020a; Guo et al., 2020; Guo et al., 2021). Among different photocatalysis materials. Bismuth vanadium oxide (BiVO₄), as an *n*-type semiconductor with a narrow bandgap, has been considered as a promising visible light semiconductor catalyst due to its non-toxicity, low price, good chemical stability and response to visible light (Lu et al., 2018). Over the years, various efforts have been made to enhance the photocatalytic activity of BiVO₄, such as morphology control (Zhang et al., 2018), noble metal modification (Zhu et al., 2020), element-doping (Regmi et al., 2017), forming heterojunction (Singh et al., 2016), and so on. Theoretically, the construction of heterojunction composite photocatalyst is the most convenient and effective method to improve the photocatalytic performance of photocatalytic materials. Compare with type II and p-n heterojunction, Z-scheme heterojunction has a unique advantage that can retain the prominent redox potential of each semiconductor photocatalyst (Lu et al., 2022b). Successful cases, ZnIn₂S₄/Ag₆Si₂O₇ (Kong et al., 2021), NiFe₂O₄/Ag₃VO₄/Ag₂VO₂PO₄ (Su et al., 2021), MoSe₂@Bi₂S₃/CdS (Wang et al., 2021a), PCN-Sb₂MoO₆-Bi₂O₃ (Zhang et al., 2021a), Bi₂WO₆/GQDs/WO₃ (Zhou et al., 2020), and so on. With the in-depth study of Z-scheme, S-scheme, which combines the advantages of Z-scheme, has become the research target of many researchers in recent years. S-scheme can accelerate the separation and transfer of interfacial charge, and give the photocatalysis better redox ability. Successful cases, Ni₂P modified step-scheme SnNb₂O₆/CdS-diethylenetriamine (Hu et al., 2020), CdSe/SnNb₂O₆ S-scheme heterojunction (Ke et al., 2021), Bi₂S₃/BiVO₄/Mn_{0.5}Cd_{0.5} ternary S-scheme heterojunction (Zhao et al., 2022), TaON/Bi₂MoO₆ core-shell S-scheme heterojunction (Li et al., 2022b), Step-scheme g-C₃N₄/Zn_{0.2}Cd_{0.8}S-DETA composites (Mei et al., 2020), and so on.

ZnIn₂S₄ is a new type ternary sulfide photocatalyst with a narrow band gap, which has excellent photochemical conversion and stable physical chemical capabilities. More importantly, ZnIn₂S₄ has a negative valence band position can suit well to catalysts with positive conduction bands to form Z-scheme heterojunction, which makes it possible to effectively promote the separation of photogenerated charges and retain the prominent redox potential (Jo et al., 2016). Zhang et al. synthesis 2D/1D Z scheme CeO₂/ZnIn₂S₄ by growing ZnIn₂S₄ nanosheets in situ on the surfaces of CeO₂ nanorods (Zhang et al., 2020b), which could enhance the photocatalytic performance of aromatic alcohols and hydrogen evolution. Furthermore, a serious of ZnIn₂S₄-based Z-scheme heterojunction has been construct, such as Cu₃P/ZnIn₂S₄ (Yang et al., 2020), ZnIn₂S₄/Nb₂O₅ (Wang et al., 2020a), ZnIn₂S₄/LaNiO₃ (Wang et al., 2020b), and so on. In addition, there are many studies on ZnIn₂S₄/BiVO₄, such as ZnIn₂S₄/BiVO₄ for efficient CO₂ photoreduction (Han et al., 2021), ZnIn₂S₄/BiVO₄ for organics degradation (Yuan et al., 2020), and so on.

AgI is an outstanding photosensitive material, with a suitable forbidden band width (~2.8 eV), which has potential performance in photocatalysis. However, the large particle size and poor stability also

limits its practical application (Chen et al., 2013; Liang et al., 2015; Wang et al., 2016). Fortunately, after loading AgI particles on other photocatalyst can form heterojunction, such as AgI-Bi₂WO₆ (Xue et al., 2019), AgI/β-Ag₂MoO₄ (Zhang et al., 2017), AgI/BiVO₄ (Chen et al., 2016), Ag₃VO₄/AgI (Zhang et al., 2018b), AgI/BiO₂COOH (Li et al., 2018), which could enhance the stability and photocatalytic activity of pure AgI. Moreover, dual Z-scheme photocatalyst with a higher photocatalytic activity than normal Z-scheme photocatalyst. For example, Zhang et al. prepared ternary AgI/LaFeO₃/g-C₃N₄ dual Z-scheme composite by ultrasound-assisted hydrothermal approach, and had an obviously enhanced photocatalytic degradation of norfloxacin (Zhang et al., 2020c). Therefore, Combine the band structure respective strengths of AgI, ZnIn₂S₄ and BiVO₄, a ternary AgI/ZnIn₂S₄/BiVO₄ dual Z-scheme composite photocatalyst was constructed to improve the migration and separation of charge for efficient photocatalytic performance with following dual Z-Scheme pathways.

Herein, the ternary AgI/ZnIn₂S₄/BiVO₄ dual Z-scheme heterojunction was successfully synthesized by hydrothermal method and in-situ precipitation method. The structure and properties of AgI/ZnIn₂S₄/BiVO₄ heterojunction were analyzed by a series of characterizations. Tetracycline (TC) was selected as the target organic pollutant to evaluate the photocatalytic activity of the as-synthesized photocatalyst under visible light irradiation. In addition, the stability of the composite photocatalyst was studied through cyclic experiments. Moreover, the possible degradation mechanism was discussed. Subsequently, this AgI/ZnIn₂S₄/BiVO₄ photocatalyst has provided a novel route to fabricate dual Z-scheme heterojunctions for the practical application of effective environment remediation.

2. Materials and methods

2.1. Synthesis of ZnIn₂S₄, BiVO₄ and ZnIn₂S₄/BiVO₄ composites and AgI/ZnIn₂S₄/BiVO₄ composite photocatalyst

All chemicals used in the present work were analytical grade and were used without any further modification. 0.378 mmol Zn(CH₃COO)₂·2H₂O, 0.756 mmol In(NO₃)₃·4H₂O and 3 mmol C₃H₇NO₂S were dissolved in 50 mL of deionized water. After magnetically stirring for 30 min, the mixed solution was transferred to Teflon-lined stainless-steel vessel and heated at 180 °C for 12 h. After cooling to the ambient temperature, the products were washed with deionized water and absolute ethanol, and vacuum dried at 60 °C for 12 h. The obtained powder was collected and named as ZIS.

4.85 g Bi(NO₃)₃·5H₂O was dissolved in 40 mL deionized water to form A solution, 1.17 g NH₄VO₃ was dissolved in 30 mL deionized water to form B solution. Stirring separately until completely dissolved, solution B was transferred to solution A. Then, 2 g SDS and a certain amount of ZIS were added into the above solutions, and the mixed solution was stirred for 30 min. Subsequently, the mixed solution was transferred to Teflon-lined stainless-steel vessel, then heated at 180 °C and kept for 24 h. The obtained products were washed several times with deionized water and ethanol. After drying at

60 °C, the $\text{ZnIn}_2\text{S}_4/\text{BiVO}_4$ composite was obtained and marked as ZB. Pure BiVO_4 was prepared without ZnIn_2S_4 and named as BVO.

5 mmol AgNO_3 and KI was dissolved in 30 mL deionized water to form solution A and B, respectively. ZB was added into solution A at a molar ratio of Bi to Ag of 5:1, 2:1, 1:1, and 1:2, respectively. Stirring separately for 3 h until completely dissolved, and then solution B was transferred to solution A. Then, stirring in the dark for 3 h. Then the resulting precipitate was centrifuged, washed with deionized water and dried at 60 °C for 12 h in the oven. The molar ratios of Bi to Ag of 5:1, 2:1, 1:1, and 1:2 in composites were record the samples as AZB 5, AZB2, AZB1 and AZB0.5, respectively. Pure AI was prepared without ZB named as AI.

The schematic illustration of preparation procedure of AZB heterojunction photocatalyst was shown in Scheme 1.

2.2. Photocatalytic performance tests

The photocatalytic activity of the as-synthesized samples was evaluated by the degradation of TC under visible light. In a traditional draft, 30 mg photocatalyst was dispersed in 50 mL 20 mg/L TC solution. Then, the mixture has been executed by magnetically stirring for 30 min in the dark to achieve absorption–desorption equilibrium before 300 W Xenon lamp ($\lambda > 420$ nm) turned on. After the dark reaction, the Xenon lamp is turned on to start the photocatalytic reaction. (4) mL of the solution were collected every 15 min during the photoreaction. After centrifugation, the supernatant was collected. Then, the concentration of TC in the supernatant was analysed by an ultraviolet–visible spectrophotometer at $\lambda = 356$ nm. The degradation rate was calculated by the following formula:

$$\text{Degradation (\%)} = [(1 - C_i/C_0)] \times 100\%$$

Where C_0 is the absorbance of the initial solution and C_i is the absorbance of the solution after the reaction.

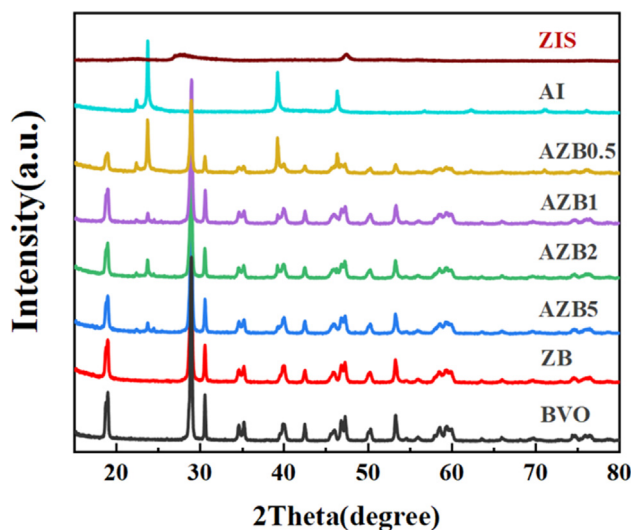


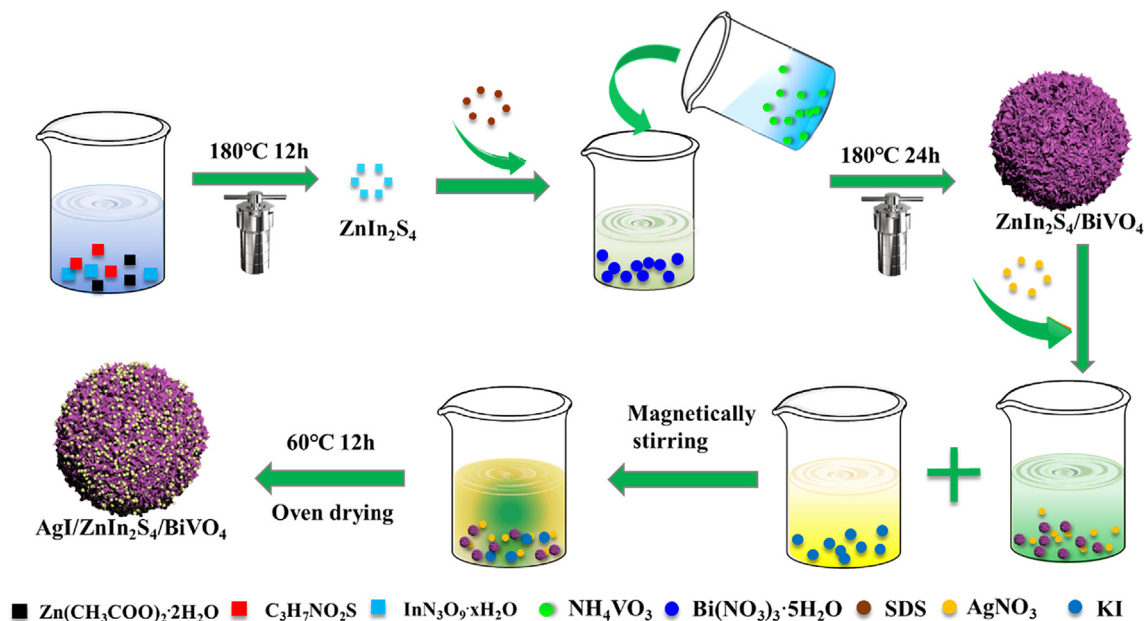
Fig. 1 XRD patterns of as-prepared samples.

2.3. Capturing experiment

Similar with the photocatalytic tests, 1 mmol IPA, 1 mmol EDTA-2Na, and 1 mmol BQ were used to conduct active species trapping tests to capture the hydroxyl radicals ($\bullet\text{OH}$), photogenerated holes (h^+) and superoxide anion radicals ($\bullet\text{O}_2^-$), respectively. The detailed information about characterization is listed in Supporting Information.

3. Results and discussion

The XRD diffraction patterns of as-synthesized photocatalysts were displayed in Fig. 1. All the diffraction peaks of pure BVO, ZIS and AI were obviously assigned to the monoclinic phase BVO (JCPDS NO.14-0688) (Wang et al., 2021b), hexagonal phase ZIS (JCPDS NO. 65-2023) (Wang et al., 2022) and



Scheme 1 Schematic of $\text{AgI}/\text{ZnIn}_2\text{S}_4/\text{BiVO}_4$ heterojunctions photocatalyst preparation.

cubic phase AI (JCPDS NO.09-0399) (Guo et al., 2018), respectively. After the recombination of BVO and ZIS, the ZB materials maintains the monoclinic phase BVO, and the ZIS diffraction peak at 27.7° and 47.5° were close to the BVO diffraction peak at 28.9° and 47.3° , which led to the overlap of above peaks. Moreover, the intensity of these diffraction peaks gradually strengthened with the increasing mass ratio of AI. Similarly, as the AI composite ratio increases, the BVO diffraction peak in AZB samples become weaker than that of pure BVO. Furthermore, no other impurity peak was observed in AZB samples meant the well purity and crystallinity, indicating the successfully synthesis of AZB heterostructure.

As displayed in Fig. 2, SEM was employed to investigate the morphology and structure of the as-synthesized photocat-

alysts. In Fig. 2a, pure BVO microspheres are formed by fast and tight combination of irregular nano-particles with an average radius of about $2\ \mu\text{m}$. As shown in Fig. 2b, the ZnIn_2S_4 possessed a micron flower with the radius of $1.5\text{--}2\ \mu\text{m}$, which was composed of numerous nanosheets. In Fig. 2c, AI possessed the fusiform with the radius of $300\ \text{nm}$. After combing ZIS with BVO, it can be clearly seen that ZIS was wrapped in microspheric BVO with a radius of $2\ \mu\text{m}$ to form ZB. In Fig. 2d, the surface and voids of ZB sample were effectively wrapped by AI particles, making the surface of the AZB nanocomposites heterojunction rougher than that of pure BVO, ZIS, AI and ZB samples. Subsequently, the intricate crystal structures of AZB were investigated by TEM and HR-TEM. In Fig. 2e, and a large number of AI particles are

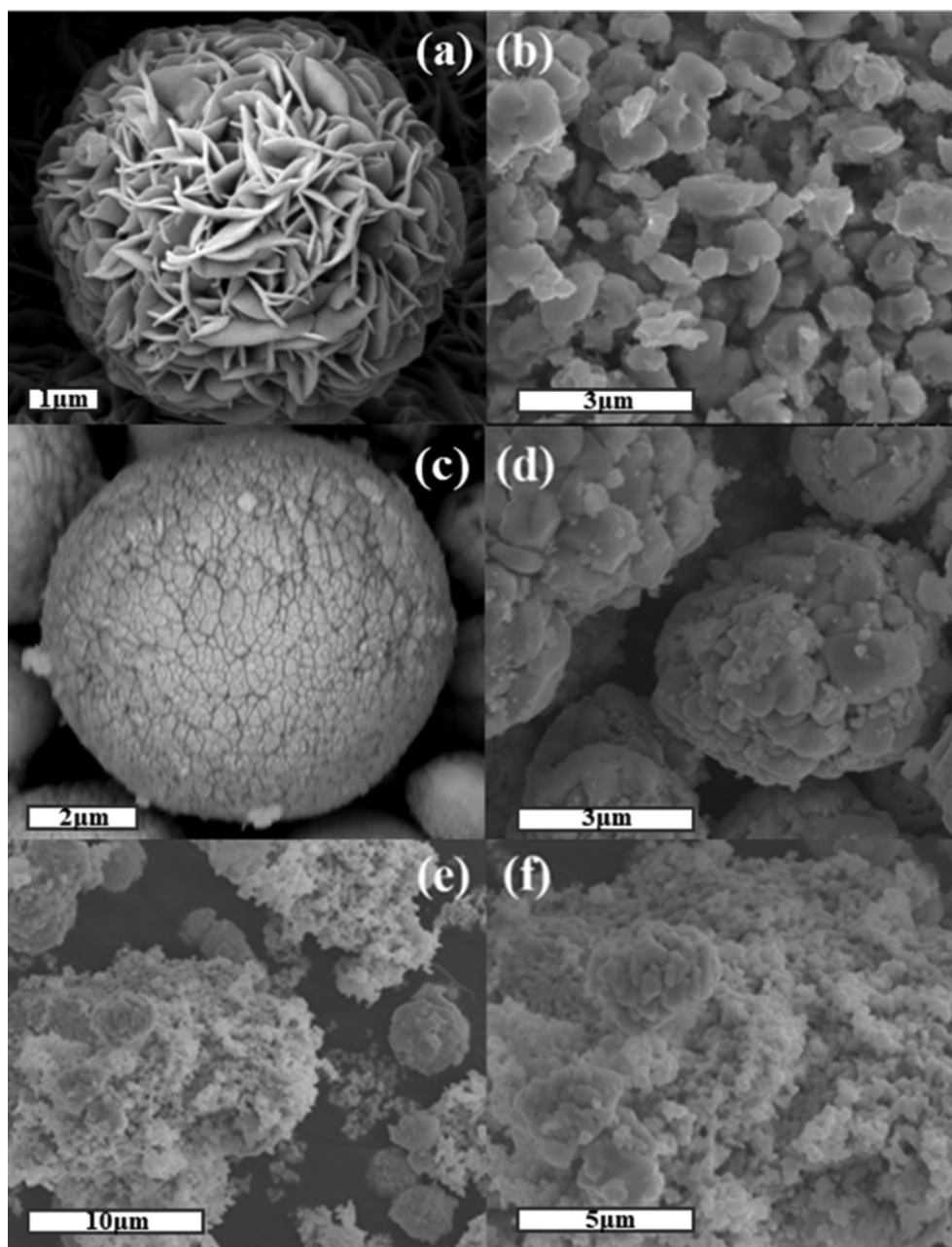


Fig. 2 SEM images of (a) ZnIn_2S_4 , (b) AgI, (c) (d) ZB, (e) (f) AZB1.

wrapped on the surface of ZB samples with close contact between the components, which shows that ZIS were well attached to the AI.

The microstructure of AZB nanocomposites was further studied by transmission electron microscopy (TEM) and high resolution transmission electron microscopy (HRTEM). TEM images of AZB1 composite in Fig. 3a and 3b clearly show that AI nanoparticles are well dispersed on the surface

of ZB microspheres. Fig. 3c is the high-resolution HRTEM image of AZB. Three types of lattice fringes with a lattice spacing of 0.230 nm, 0.308 nm and 0.322 nm can be observed, corresponding to the (200) crystal plane of AI (Chen et al., 2019), the (121) crystal plane of BVO (Pham et al., 2020) and (102) crystal plane of ZIS (Hussain et al., 2020), respectively. In addition, Fig. 3d shows the element plot of the AZB1 composite, showing a uniform spatial distribution of the Ag, I, Zn, In,

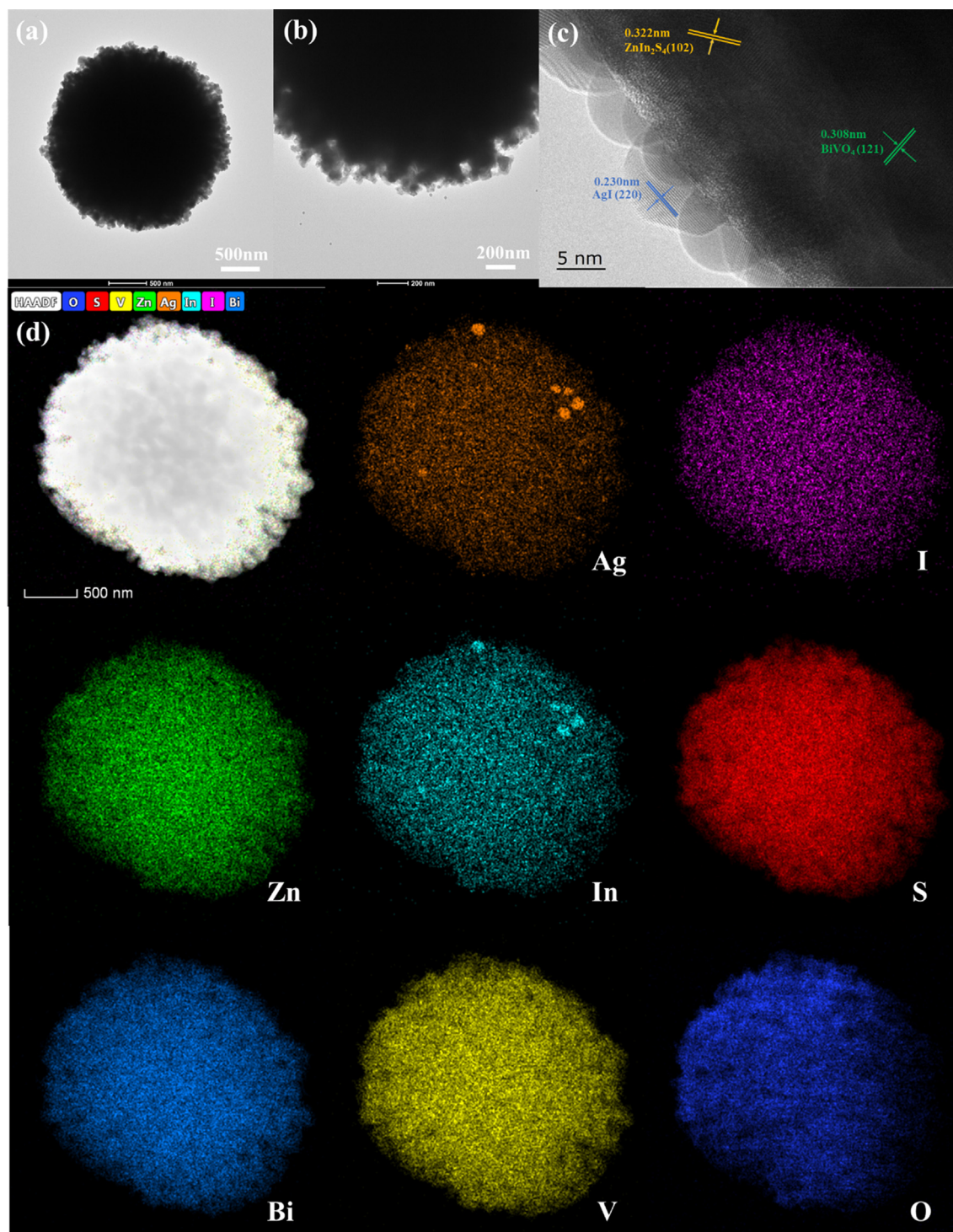


Fig. 3 (a, b) TEM and (c) HRTEM images images of AZB1 sample. (d) HAADF and elemental mapping images of AZB1 sample.

S, Bi, V and O elements, consistent with the element in AZB composite, further indicating a successful synthesis of the AZB composite. In addition, Fig. S1 demonstrated the N_2 adsorption-desorption isotherms and the corresponding pore size distribution of as-prepared AZB1 sample. The BET surface area, pore volume and average pore diameter of AZB1, were $2.0525 \text{ m}^2 \text{ g}^{-1}$, $0.012170 \text{ cm}^3 \text{ g}^{-1}$ and 22.2033 nm , which were also summarized in Fig. S1.

XPS spectra were conducted to exhibit the composition and valence of chemical elements of the as-prepared AZB1, AI, ZIS and BVO samples. Fig. 4a and 4b, displayed the survey spectra of AZB1, AI, ZIS and BVO, which indicated the as-prepared samples consists of their own elements and no other elements existed. In Fig. 4c, the diffraction peaks of S 2p and Bi 4f was overlapped around the region of 160 eV. After analysis by $2j + 1$ condition typical constraints of the spin-orbit splitting (Morales-Lun et al., 2017), Bi 4f can be divided into two diffraction peaks Bi 4f_{7/2} and Bi 4f_{5/2}, respectively found at 159.4 eV and 164.1 eV. Meanwhile, it was also possible to deconvolve two diffraction peaks of S 2p_{3/2} and S 2p_{1/2} at 160.5 eV and 162.3 eV, confirm that the Bi element and S element were Bi³⁺ and S²⁻ in the sample (Lu et al., 2019). Compared with ZIS and BVO, the XPS spectra peaks of Bi 4f and S 2p had a slightly shift to positive position. Fig. 4d showed the

V 2p XPS spectrum, the binding energy peaks of AZB1 at 517.0 eV, 524.2 eV and of BVO at 516.7 eV and 524.1 eV corresponded to V 2p_{3/2} and V 2p_{1/2}, respectively, proving that the V element was existence of + 5 valence (Wang et al., 2021b). From Fig. 4e, the high-resolution spectrum of Zn 2p_{3/2} as well as Zn 2p_{1/2} at 1025.1 eV and 1022.0 eV indicated Zn²⁺. Similarly, it can be known that Zn²⁺ exist in ZIS and AZB1. In Fig. 4f, the band energy of In 3d at 441.9 eV, 452.6 eV and 442.0 eV, 452.7 eV were corresponded to In 3d_{5/2} and In 3d_{3/2}, respectively, proving the presence of In³⁺ in ZnIn₂S₄ and AZB1. From Fig. 4g, two characteristic peaks of Ag 3d_{5/2} and Ag 3d_{3/2} were located at a binding energy of 368.4 eV, 374.3 eV and 368.6 eV, 374.5 eV, which proved the existence of Ag⁺. Fig. 4h showed the characteristic diffraction peaks at 619.3 eV and 630.7 eV, corresponded to I 3d_{5/2} and I 3d_{3/2}, respectively. Same argument the characteristic diffraction peaks at 619.3 eV and 630.7 eV, corresponding to I 3d_{5/2} and I 3d_{3/2} in the AI. In Fig. 4i, the diffraction peak of ABZ1 at the binding energy of 530.7 eV is the characteristic peak of O 1s, which was respectively attributed to lattice oxygen in Bi-O (529.8 eV), V-O (531.8 eV) and O-H (530.4 eV) adsorbed on the surface (Gao et al., 2017). For BVO, O 1s spectrum peaks at 528.2 eV and 530.0 eV, corresponding to the lattice oxygen and surface-adsorbed oxygen species. In

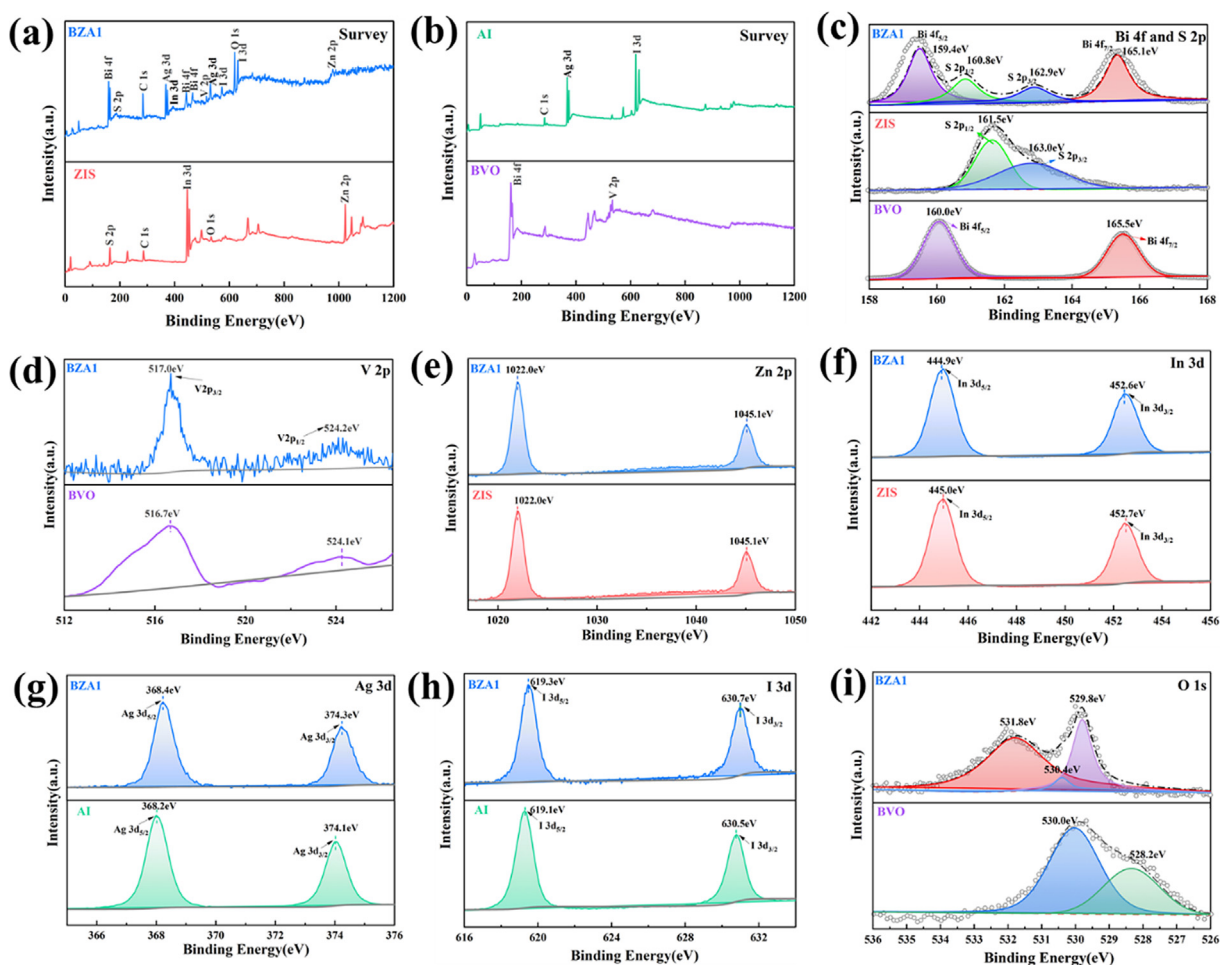


Fig. 4 XPS spectrum of AZB1, AI, ZIS and BVO: (a) (b) full spectrum, (c) Bi 4f and S 2p, (d) V 2p, (e) Zn 2p, (f) In 3d, (g) Ag 3d, (h) I 3d, (i) O 1s.

summary, it could be proved that BVO, ZIS and AI coexist in the AZB sample, which was consistent with the XRD results.

UV-vis were performed to investigate the light absorption performance of as-prepared photocatalysts. As can be seen in Fig. 5a, the adsorption edges of both pure AI and BVO were up to 466 nm and 570 nm in the visible light region, which meant they can utilize visible light. Since the ZIS was black powder and the absorption of light was strong, the ZB and AZB1 samples combined with ZIS could absorb more light in the visible region than pure AI and BVO, indicating that the composite photocatalytic system had a strong responsibility in the visible light region. The band gap energy of as-prepared samples was calculated by Tauc equation (Zhang et al., 2021b) and displayed in Fig. 5b. Since BiVO₄, AI and ZIS were direct bandgap semiconductors ($n = 1$ for direct transition), the calculated E_g of them were 2.40 eV, 2.70 eV and 2.20 eV, respectively. The positions of valence band were conducted by the positions of conduction band and valence band. In Fig. 5c, the E_{VB} of BiVO₄, AI and ZIS were 2.76 V, 2.36 V and 1.66 V (vs NHE), respectively. Further, the conduction bands of BVO, AgI and ZIS could be calculated as 0.32 V, -0.34 V and -0.54 V, respectively.

The photocatalytic activity of the as-prepared samples was evaluated by photodegradation of TC under visible light irradiation. In Fig. 6a, that TC wastewater was hard to degrade under light without photocatalyst, indicating TC had good stability under light irradiation. The TC removal efficiency of

pure BiVO₄, AgI and ZIS only 42.11 %, 60.71 % and 54.19 % in 2 h, respectively. After combined with AgI and ZnIn₂S₄, the composite photocatalyst inhibited the recombination of photo-generated electrons and holes, and accelerated the conduction speed of the photo-generated carriers in the composite. The photocatalytic activity of AZB composite photocatalysts was higher than that of pure BVO, AgI and ZIS, indicating that the photocatalytic performance of the sample has been significantly improved. Furthermore, with the increasing ratio of AI, the degradation rate of TC wastewater for AZB composite photocatalysts increased firstly. Among them, AZB1 had the best photocatalytic activity for TC wastewater, with the degradation rate of TC up to 91.44 %. When the composite ratio of AI continued to increase, the decrease of photocatalytic activity can be attributed to the weakness of the synergistic effect among BiVO₄, AI and ZIS. Moreover, all photocatalytic reactions performed conform to the first-order reaction kinetic equation in Fig. 6b. The reaction rate constants for BVO, AI, ZIS, ZB, AZB5, AZB2, AZB1 and AZB0.5 were 0.00452, 0.00647, 0.00648, 0.00633, 0.00949, 0.01395, 0.02118 and 0.01329 min^{-1} . The reaction rate of the AZB1 composite photocatalyst was 4.68, 3.27 and 3.27 times higher than that of pure BVO, AI, and ZIS, indicating that the synergistic effect among BVO, AI, and ZIS could improve the photocatalytic properties. In addition to photocatalytic efficiency, TOC and COD removal are also very important performance for photocatalyst. As shown in

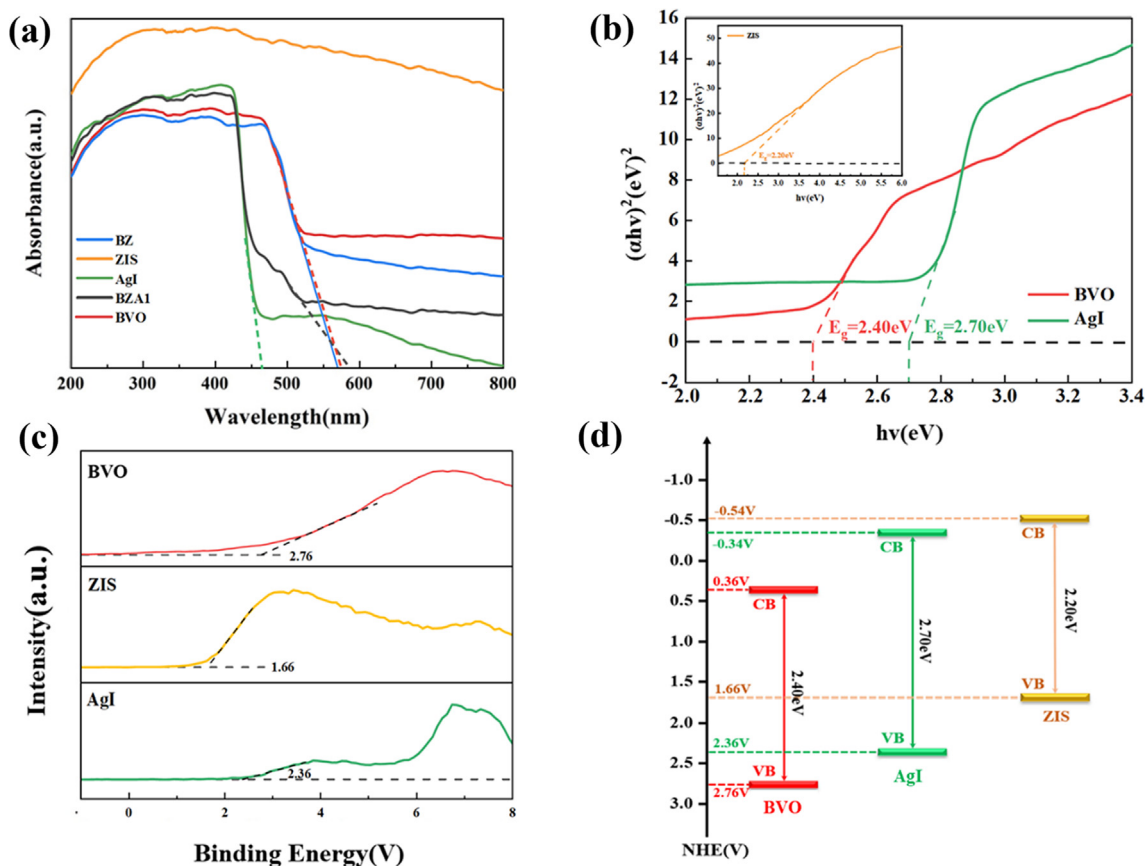


Fig. 5 (a) UV-vis of as-prepared samples, (b) Plots of $(\alpha h\nu)^2$ against photon energy ($h\nu$), XPS valence band spectra and the calculated bandgap of AI, ZIS and BVO.

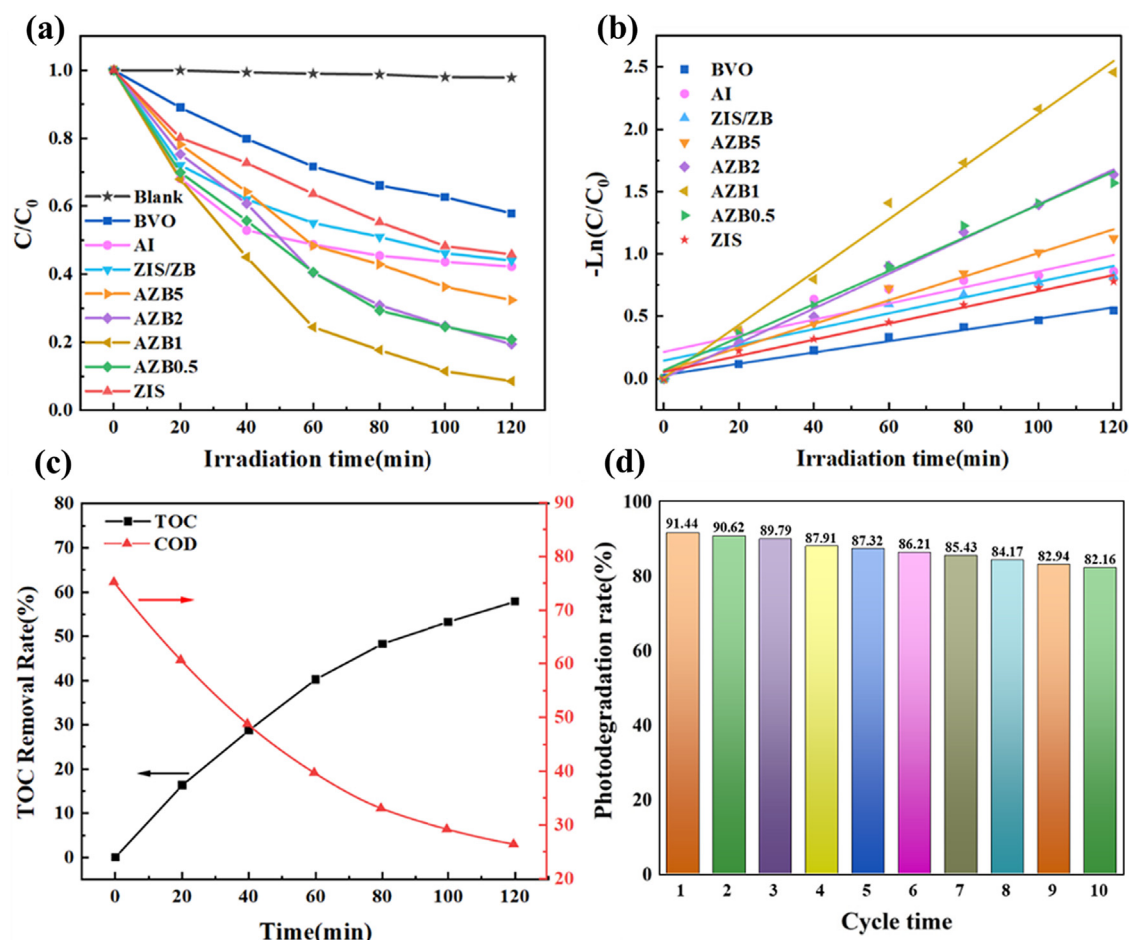


Fig. 6 (a) The photocatalytic activity for TC of the as-prepared samples under visible light irradiation, (b) first-order reaction kinetics of photocatalytic degradation of TC, (c) The TOC and COD removal curve of AZB1 sample for TC degradation, (d) Ten cycles curve of AZB1 sample for TC degradation.

Fig. 6c, the TOC and COD removal efficiency of AZB1 samples were 57.85 % and 64.89 %, respectively, which were lower than photocatalytic properties. This is because TC in the solution does not completely degrade into inorganic substances, but existed as intermediate. Moreover, the stability and repetitiveness of photocatalysts were significant for practical application. As shown in Fig. 6d, AZB1 still remained high degradation rate (82.16 %) for TC wastewater after 10 cycles, which was only about 9 % lower than that of the first time. The above results prove that the formation of AZB composite heterojunction effectively inhibits the photo-corrosion phenomenon of the catalyst, and has excellent photocatalytic stability and recyclability.

Transient photocurrent response and electrochemical impedance spectra were employed to analyze the generation and separation efficiency. As illustrated in Fig. 7a, the photocurrent response of AZB1 was much stronger than that of pure BVO, AI, and ZIS, indicating that more photo-generated carriers were generated (Zhou et al., 2021). Moreover, the EIS Nyquist plots were opposite to the photocurrent intensity which mean the AZB composite photocatalyst had the fastest photo-generated electron transfer efficiency. From the above results, it was drawn that the AZB could inhibit the

recombination of photo-generated carriers and accelerate the migration rate of photo-generated electrons.

To verify photocatalytic mechanism, active radical capturing experiments and electron spin resonance (ESR) spectroscopy were employed to explore the role of $\bullet\text{O}_2^-$, h^+ , and $\bullet\text{OH}$ in Fig. 8. BQ, EDTA-2Na and IPA were selected as trapping agents and added into the reaction system capture $\bullet\text{O}_2^-$, h^+ , and $\bullet\text{OH}$, respectively. It can be seen from Fig. 8(a) after adding BQ, the removal rate of TC was reduced to 41.76 %, indicated that $\bullet\text{O}_2^-$ also played a certain role in the degradation process. After adding trapping agent EDTA-2Na, the photodegradation efficiency was significantly inhibited (32.51 %), indicated that h^+ played an important role in the photocatalytic degradation reaction. Moreover, the degradation effect of TC solution was decreased to 52.39 % after the addition of IPA capture agent, which indicated that $\bullet\text{OH}$ was also exist as the main active group. Since capturing h^+ also inhibit the generation of $\bullet\text{OH}$, the photodegradation efficiency of adding EDTA-2Na is slightly higher than adding IPA, indicating h^+ directly oxidize a small amount of TC. The above results indicated that h^+ , $\bullet\text{O}_2^-$ and $\bullet\text{OH}$ were all involved in the reaction system for photocatalytic degradation of TC solution, and $\bullet\text{O}_2^-$ and $\bullet\text{O}_2^-$ were the main active species.

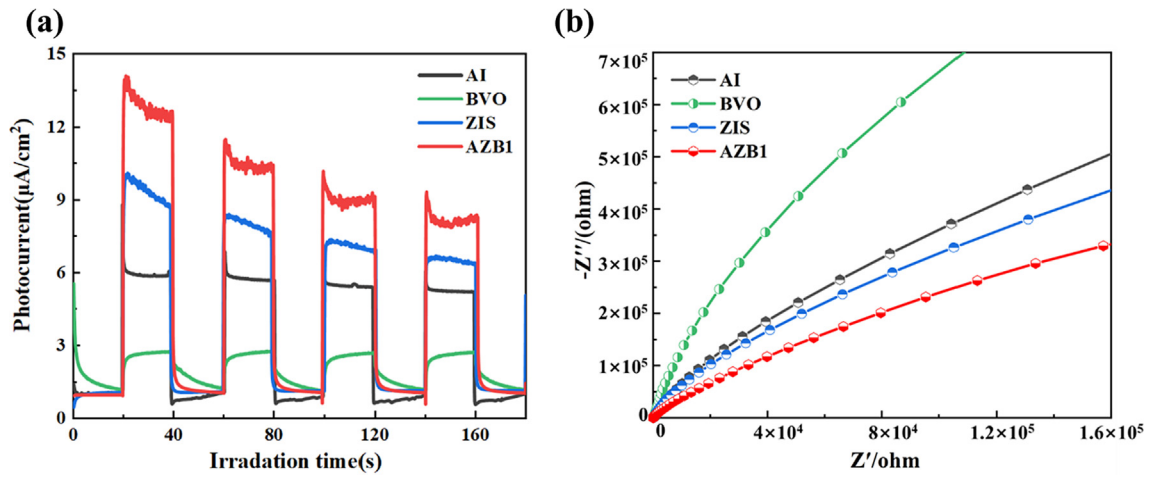


Fig. 7 (a) Transient photocurrent responses and (b) EIS plots of BiVO₄ \ AgI \ ZIS and AZB1 samples.

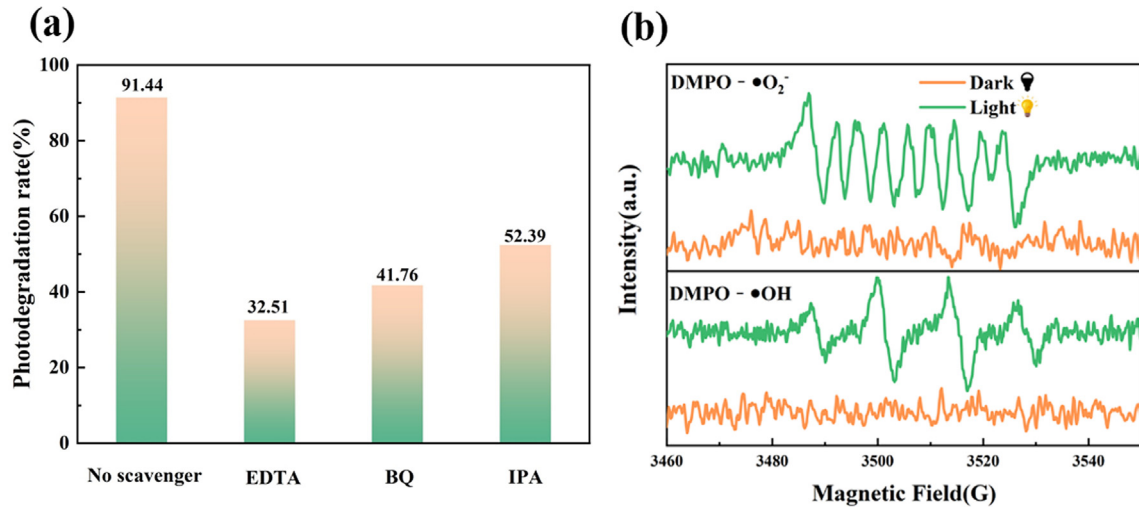
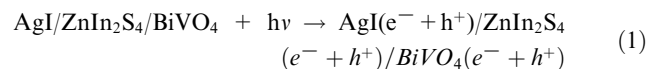


Fig. 8 (a) DMPO spin-trapping ESR spectra over AZB1 samples under dark and visible light condition for DMPO- $\bullet\text{O}_2^-$ and DMPO- $\bullet\text{OH}$, (b). The effect of different quenchers on the TC degradation by AZB1 photocatalysts.

To further verify the existence of free radicals, the ESR analysis was performed under visible light. As shown in Fig. 8b, no EPR signals regular of DMPO- $\bullet\text{O}_2^-$ and DMPO- $\bullet\text{OH}$ was observed under dark conditions. However, a series of obvious characteristic peaks was received under light conditions, indicating that $\bullet\text{O}_2^-$ and $\bullet\text{OH}$ free radicals were involved and played critical roles in photocatalytic reactions (Li et al., 2020).

According to the above results, the probable photocatalytic mechanism of AZB heterojunction was recommended in Fig. 9. If no interfacial effect was recognized after the construction of AZB heterojunction, the dual type-II photocatalytic mechanism was referred as shown in Fig. 9a. Under light illumination, the photoinduced electrons would shift from the CB of ZIS to the CB of AI then to CB of BVO. On the contrary, the photogenerated h^+ will transfer from the VB of BVO to the VB of AI then to VB of ZIS. However, the CB potential of BVO (vs NHE, 0.32 V) is more positive than that of $\text{O}_2/\bullet\text{O}_2^-$ (-0.33 V vs NHE) and the VB potential of ZIS is more negative than that of $\text{OH}^-/\bullet\text{OH}$ (2.40 V vs

NHE), indicating no $\bullet\text{O}_2^-$ and $\bullet\text{OH}$ was achieved, which is not consistent with ESR results (Shi et al., 2022). In Fig. 9b, if AZB heterojunction followed dual Z-scheme heterojunction, the photoelectrons on the CB position of AI and ZIS can move to the VB of ZIS and BVO via the Z-scheme route, respectively. Simultaneously, leaving the h^+ on the VB of BVO (2.76 V vs NHE) and e^- on the CB of ZIS (-0.54 V vs NHE), $\bullet\text{O}_2^-$ and $\bullet\text{OH}$ were generated in photocatalysis reaction. Therefore, $\bullet\text{O}_2^-$ and $\bullet\text{OH}$ should be the main active species, and h^+ is also participating in the reaction and directly degrade TC, which was consistent with the result of active species trapping. This dual Z-scheme heterojunction not only effectively promote the separation of photogenerated charges, but also retain the prominent redox potential. Finally, the photocatalytic degradation process of TC by AZB was described as follows:



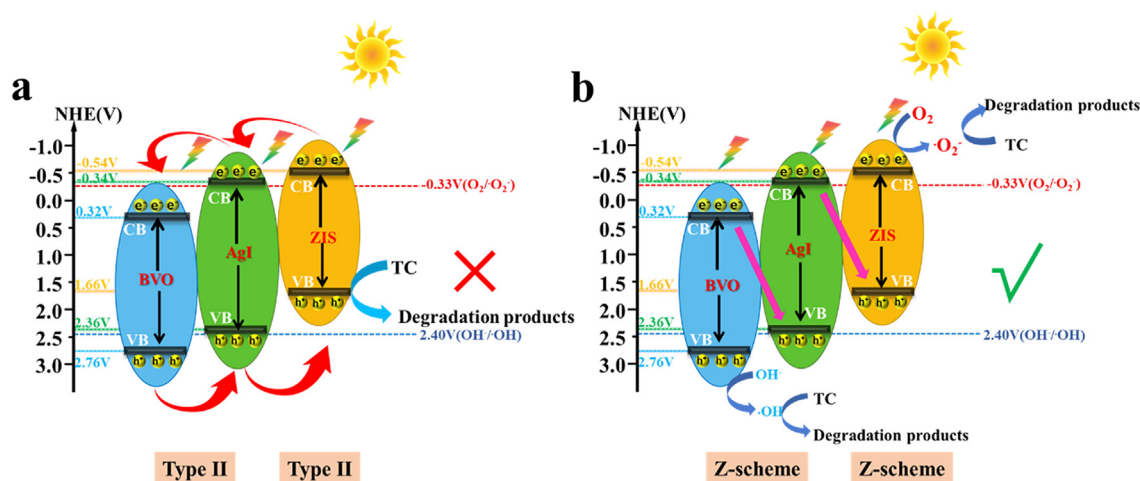
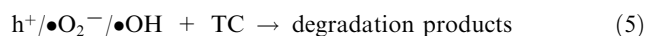
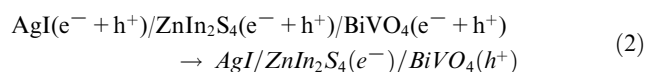


Fig. 9 The probable the photocatalytic mechanism of TC over AZB heterojunction.



4. Conclusions

In summary, a novel ternary AgI/ZnIn₂S₄/BiVO₄ dual Z-scheme heterojunction was successfully synthesized by hydrothermal method and in-situ precipitation method. Subsequently, the morphology, crystal structure, elemental composition analyses, composition and photoelectrochemical properties, as well as the charge carriers transfer mechanism of AgI/ZnIn₂S₄/BiVO₄ dual Z-scheme heterojunction have been explored in detail. AgI/ZnIn₂S₄/BiVO₄ heterojunction showed higher photocatalytic activity than that of pure AgI, ZnIn₂S₄ and BiVO₄ towards degradation of TC. In addition, the most excellent photocatalytic activity was obtained by the molar ratio of Bi to Ag in the heterostructure is 1:1, which can be attributed to the formation of dual Z-scheme heterojunction effectively promotes the separation and transfer of photogenerated electron-hole pairs and greatly extends the life of carriers. Finally, a probable photocatalytic mechanism of AZB heterojunction with dual Z-scheme pathways were recommended by ESR and active species trapping experiments. The present work suggested a promising approach for the design of ternary dual Z-scheme heterojunction with multilevel electron transfer to present greater photo-absorption, charge separation, and photodegradation for environmental decontamination.

Declaration of Competing Interest

The authors declare that they have no known competing financial interests or personal relationships that could have appeared to influence the work reported in this paper.

Acknowledgements

This work is supported by the National Natural Science Foundation of China (21906039 and 52000024, China),

Shanghai Sailing Program (20YF1400300, China), Hebei Province 333 Talents Project (A202101020, China), Natural Science Foundation of Shaanxi Province (2019JYM-429, China), Funding Project for Introduced Overseas Scholars of Hebei Province (C20190321, China), Science and Technology Project of Hebei Education Department (BJ2021010, China), Program for water resources research and promotion of Hebei Province (2019-55, China), Fundamental Research Funds for the Central Universities of Chang'an University (310829172002, 300102298104, 300102290501, China) and Donghua University, Basic Scientific Research Funds for Universities of Hebei Province and Student Science and Technology Foundation of Hebei GEO University (KAG202205, China), Doctoral research fund of Hebei Geo University (BQ2019041, China).

Appendix A. Supplementary material

Supplementary data to this article can be found online at <https://doi.org/10.1016/j.arabj.2022.104159>.

References

- Chen, L.L., Jiang, D.L., Tong, H., Wu, Z.D., Chen, M., 2013. In-situ ion exchange synthesis of hierarchical AgI/BiOI microsphere photocatalyst with enhanced photocatalytic properties. *Crystengcomm.* 15, 7556–7563. <https://doi.org/10.1039/C3CE41038B>.
- Chen, J.Y., Xiao, X.Y., Wang, Y., Lu, M.L., Zeng, X.Y., 2019. Novel AgI/BiOBr/reduced graphene oxide Z-scheme photocatalytic system for efficient degradation of tetracycline. *J. Alloy. Compd.* 800, 88–98. <https://doi.org/10.1016/j.jallcom.2019.06.004>.
- Chen, F., Yang, Q., Sun, J., Yao, F.B., Wang, S.N., Wang, Y.L., Wang, X.L., Li, X.M., Niu, C.G., Wang, D.B., Zeng, G.M., 2016. Enhanced photocatalytic degradation of tetracycline by AgI/BiVO₄ heterojunction under visible-light irradiation: mineralization efficiency and mechanism. *ACS Appl. Mater. Interfaces* 8, 32887–32900. <https://doi.org/10.1021/acsami.6b12278>.
- Gao, S.W., Guo, C.S., Hou, S., Wan, L., Wang, Q., Lv, J.P., Zhang, Y., Gao, J.F., Meng, W., Xu, J., 2017. Photocatalytic removal of tetrabromobisphenol A by magnetically separable flower-like BiOBr/BiOI/Fe₃O₄ hybrid nanocomposites under visible-light irradiation. *J. Hazard. Mater.* 331, 1–12. <https://doi.org/10.1016/j.jhazmat.2017.02.030>.

- Guo, F., Shi, W.L., Wang, H.B., Han, M.M., Guan, W.S., Huang, H., Liu, Y., Kang, Z.H., 2018. Study on highly enhanced photocatalytic tetracycline degradation of type II AgI/CuBi₂O₄ and Z-scheme AgBr/CuBi₂O₄ heterojunction photocatalysts. *J. Hazard. Mater.* 349, 111–118. <https://doi.org/10.1016/j.jhazmat.2018.01.042>.
- Guo, J.F., Yang, C.S., Sun, Z.X., Yang, Z., Wang, L.P., Lu, C.Y., Ma, Z.Y., Guo, F., 2020. Ternary Fe₃O₄/MoS₂/BiVO₄ nanocomposites: novel magnetically separable visible light-driven photocatalyst for efficiently degradation of antibiotic wastewater through p-n heterojunction. *J. Mater. Sci. Mater. Electron.* 31, 16746–16758. <https://doi.org/10.1007/s10854-020-04230-9>.
- Guo, J.F., Xu, Y., Li, J., Yang, C.S., Lu, C.Y., 2021. Preparation of a novel composite material LaCoO₃/Bi₂WO₆ and its application in the treatment of tetracycline. *J. Mater. Sci. Mater. Electron.* 32, 13813–13824. <https://doi.org/10.1007/s10854-021-05957-9>.
- Han, Q., Li, L., Gao, W., Shen, Y., Wang, L., Zhang, Y.T., Wang, X. Y., Shen, Q., Xiong, Y.J., Zhou, Y., Zou, Z.G., 2021. Elegant construction of ZnIn₂S₄/BiVO₄ hierarchical heterostructures as direct Z-Scheme photocatalysts for efficient CO₂ photoreduction. *ACS Appl. Mater. Interfaces* 13 (13), 15092–15100. <https://doi.org/10.1021/acsami.0c21266>.
- Hu, T.P., Dai, K., Zhang, J.F., Chen, S.F., 2020. Noble-metal-free Ni₂P modified step-scheme SnNb₂O₆/CdS-diethylenetriamine for photocatalytic hydrogen production under broadband light irradiation. *Appl. Catal. B-Environ.* 269, <https://doi.org/10.1016/j.apcatb.2020.118844> 118844.
- Hussain, M.B., Azhar, U., Loussala, H.M., Razaq, R., 2020. Synergistic effect of ZnIn₂S₄ nanosheets with metal-organic framework molding heterostructure for efficient visible-light driven photocatalytic reduction of Cr(VI). *Arab. J. Chem.* 13, 5939–5948. <https://doi.org/10.1016/j.arabjc.2020.04.029>.
- Jo, W.K., Lee, J.Y., Natarajan, T.S., 2016. Fabrication of hierarchically structured novel redox-mediator-free ZnIn₂S₄ marigold flower/Bi₂WO₆ flower-like direct Z-scheme nanocomposite photocatalysts with superior visible light photocatalytic efficiency. *Phys. Chem. Chem. Phys.* 18, 1000–1016. <https://doi.org/10.1039/C5CP06176H>.
- Ke, X.C., Zhang, J.F., Dai, K., Fan, K., Liang, C.H., 2021. Integrated S-scheme heterojunction of amine-functionalized 1D CdSe nanorods anchoring on ultrathin 2D SnNb₂O₆ nanosheets for robust solar-driven CO₂ conversion. *Solar RRL* 5 (4), 2000805. <https://doi.org/10.1002/solr.202000805>.
- Kong, D.Z., Ruan, X.X., Geng, J.K., Zhao, Y.H., Zhang, D.F., Pu, X. P., Yao, S.J., Su, C.H., 2021. 0D/3D ZnIn₂S₄/Ag₆Si₂O₇ nanocomposite with direct Z-scheme heterojunction for efficient photocatalytic H₂ evolution under visible light. *Int. J. Hydrog. Energy* 46 (55), 28043–28052. <https://doi.org/10.1016/j.ijhydene.2021.06.053>.
- Li, S.J., Chen, J.L., Hu, S.W., Jiang, W., Liu, Y.P., Liu, J.S., 2020. A novel 3D Z-scheme heterojunction photocatalyst: Ag₆Si₂O₇ anchored on flower-like Bi₂WO₆ and its excellent photocatalytic performance for the degradation of toxic pharmaceutical antibiotics. *Inorg. Chem. Front.* 7, 529–541. <https://doi.org/10.1039/C9QI01201J>.
- Li, S., Jiang, W., Xu, K.B., Hu, S.W., Liu, Y., Zhou, Y.T., Liu, J.S., 2018. Synthesis of flower-like AgI/BiOCCOOH p-n heterojunctions with enhanced visible-light photocatalytic performance for the removal of toxic pollutants. *Front. Chem.* 2018 (6), 518. <https://doi.org/10.3389/fchem.2018.00518>.
- Li, J.T., Liu, H.J., Liu, Z., Yang, D.Q., Zhang, M.Z., Gao, L.N., Zhou, Y.H., Lu, C.Y., 2022a. Facile synthesis of Z-scheme NiO/α-MoO₃ p-n heterojunction for improved photocatalytic activity towards degradation of methylene blue. *Arab. J. Chem.* 15, <https://doi.org/10.1016/j.arabjc.2021.103513> 103513.
- Li, S.J., Wang, C.C., Cai, M.J., Yang, F., Liu, Y.P., Chen, J.L., Zhang, P., Li, X., Chen, X.B., 2022b. Facile fabrication of TaON/Bi₂MoO₆ core-shell S-scheme heterojunction nanofibers for boosting visible-light catalytic levofloxacin degradation and Cr(VI) reduction. *Chem. Eng. J.* 428, <https://doi.org/10.1016/j.cej.2021.131158> 131158.
- Liang, J.L., Shan, C., Zhang, X., Tong, M.P., 2015. Bactericidal mechanism of BiOI/AgI under visible light irradiation. *Chem. Eng. J.* 279, 277–285. <https://doi.org/10.1016/j.cej.2015.05.024>.
- Lu, C.Y., Dang, J.J., Hou, C.T., Jiang, Y.J., Guan, W.S., 2018. Photocatalytic degradation of doxycycline on ellipsoid-like BiVO₄ synthesized by EDTA-assisted. *Desalination Water Treat.* 104, 250–256. <https://doi.org/10.5004/dwt.2018.21867>.
- Lu, C.Y., Guo, F., Yan, Q.Z., Zhang, Z.J., Li, D., Wang, L.P., Zhou, Y.H., 2019. Hydrothermal synthesis of type II ZnIn₂S₄/BiPO₄ heterojunction photocatalyst with dandelion-like microflower structure for enhanced photocatalytic degradation of tetracycline under simulated solar light. *J. Alloy. Compd.* 811, <https://doi.org/10.1016/j.jallcom.2019.151976> 151976.
- Lu, C.Y., Wang, L.T., Yang, D.Q., Jin, Z.H., Wang, X., Xu, J.M., Li, Z. D., Shi, W.L., Guan, W.S., Huang, W., 2022a. Boosted tetracycline and Cr(VI) simultaneous cleanup over Z-Scheme BiPO₄/CuBi₂O₄ p-n heterojunction with 0D/1D trepan-like structure under simulated sunlight irradiation. *J. Alloys Compd.* 919, <https://doi.org/10.1016/j.jallcom.2022.165849> 165849.
- Lu, C.Y., Yang, D.Q., Wang, L.T., Wen, S.J., Cao, D.L., Tu, C.Q., Gao, L.N., Li, Y.L., Zhou, Y.H., Huang, W., 2022b. Facile construction of CoO/Bi₂WO₆ p-n heterojunction with following Z-Scheme pathways for simultaneous elimination of tetracycline and Cr(VI) under visible light irradiation. *J. Alloys Compd.* 904, <https://doi.org/10.1016/j.jallcom.2022.164046> 164046.
- Mei, F. F., Li, Z., Dai, Kai, Zhang, J.F., Liang, C.H., 2020. Step-scheme porous g-g-C₃N₄/Zn_{0.2}Cd_{0.8}S-DETA composites for efficient and stable photocatalytic H₂ production. *Chinese J. Catal.* 2020, 41, 41–49. [https://doi.org/10.1016/S1872-2067\(19\)63389-9](https://doi.org/10.1016/S1872-2067(19)63389-9).
- Morales-Lun, M., Tomás, S.A., Arvizu, M.A., Pérez-González, M., Campos-Gonzalez, E., 2017. The evolution of the Mo⁵⁺ oxidation state in the thermochromic effect of MoO₃ thin films deposited by rf magnetron sputtering. *J. Alloy Compd.* 722, 938–945. <https://doi.org/10.1016/j.jallcom.2017.06.149>.
- Pham, M.Q., Ngo, T.M., Nguyen, V.H., Nong, L.X., Vo, D.N., Tran, T.V., Nguyen, T.-D., Xuan- Bui, T., Nguyen, T.D., 2020. Facile solvothermal synthesis of highly active monoclinic scheelite BiVO₄ for photocatalytic degradation of methylene blue under white LED light irradiation. *Arab. J. Chem.* 13, 8388–8394. <https://doi.org/10.1016/j.arabjc.2020.05.029>.
- Regmi, C., Kshetri, Y., Kim, T., Pandey, R., Lee, S.W., 2017. Mechanistic understanding of enhanced photocatalytic activity of N-doped BiVO₄ towards degradation of ibuprofen: an experimental and theoretical approach. *Mol. Catal.* 432, 220–231. <https://doi.org/10.1016/j.mcat.2019.03.014>.
- Shi, W.L., Wang, L.J., Wang, J., Sun, H.R., Shi, Y.X., Guo, F., Lu, C. Y., 2022. Magnetically retrievable CdS/reduced graphene oxide/ZnFe₂O₄ ternary nanocomposite for self-generated H₂O₂ towards photo-Fenton removal of tetracycline under visible light irradiation. *Sep. Purif. Technol.* 292, 120987. <https://doi.org/10.1016/j.seppur.2022.120987>.
- Singh, A.P., Kodan, N., Mehta, B.R., Held, A., Mayrhofer, L., Moseler, M., 2016. Band edge engineering in BiVO₄/TiO₂ heterostructure: enhanced photoelectrochemical performance through improved charge transfer. *Acs Catal.* 6, 5311–5318. <https://doi.org/10.1021/acscatal.6b00956>.
- Su, C.H., Zhang, D.F., Pu, X.P., He, Z., Hu, X., Li, L., Hu, G.Z., 2021. Magnetically separable NiFe₂O₄/Ag₃VO₄/Ag₂VO₂PO₄ direct Z-scheme heterostructure with enhanced visible-light photoactivity. *J. Chem. Technol. Biotechnol.* 96 (10), 2976–2985. <https://doi.org/10.1002/jctb.6855>.
- Wang, Y.W., Kong, X.G., Jiang, M.H., Zhang, F.Z., Lei, X.D., 2020a. A Z-scheme ZnIn₂S₄/Nb₂O₅ nanocomposite: constructed and used as an efficient bifunctional photocatalyst for H₂ evolution and oxidation of 5-hydroxymethylfurfural. *Inorg. Chem. Front.* 7, 437–446. <https://doi.org/10.1039/C9QI01196J>.

- Wang, X.G., Lu, Q.Y., Sun, Y., Liu, K., Cui, J.T., Lu, C.Y., Dai, H. L., 2022. Fabrication of novel p-n-p heterojunctions ternary $\text{WSe}_2/\text{In}_2\text{S}_3/\text{ZnIn}_2\text{S}_4$ to enhance visible-light photocatalytic activity. *Cryst. Growth Des.* 10, 108354. <https://doi.org/10.1016/j.jcece.2022.108354>.
- Wang, T.Y., Quan, W., Jiang, D.L., Chen, L.L., Li, D., Meng, S.C., Chen, M., 2016. Synthesis of redox-mediator-free direct Z-scheme AgI/WO_3 nanocomposite photocatalysts for the degradation of tetracycline with enhanced photocatalytic activity. *Chem. Eng. J.* 300, 280–290. <https://doi.org/10.1016/j.cej.2016.04.128>.
- Wang, Z.Y., Su, B., Xu, J.L., Hou, Y.D., Ding, Z.X., 2020b. Direct Z-scheme $\text{ZnIn}_2\text{S}_4/\text{LaNiO}_3$ nanohybrid with enhanced photocatalytic performance for H_2 evolution. *Int. J. Hydrogen Energy* 45, 4113–4121. <https://doi.org/10.1016/j.ijhydene.2019.12.077>.
- Wang, K., Xing, Z.P., Meng, D., Zhang, S.Y., Li, Z.Z., Pan, K., Zhou, W., 2021a. Hollow $\text{MoSe}_2@/\text{Bi}_2\text{S}_3/\text{CdS}$ core-shell nanostructure as dual Z-scheme heterojunctions with enhanced full spectrum photocatalytic-photothermal performance. *Appl. Catal. B-Environ.* 281. <https://doi.org/10.1016/j.apcatb.2020.119482>.
- Wang, S.H., Zhao, L., Huang, W., Zhao, H., Chen, J.Y., Cai, Q., Jiang, X., Lu, C.Y., Shi, W.L., 2021b. Solvothermal synthesis of CoO/BiVO_4 p-n heterojunction with micro-nano spherical structure for enhanced visible light photocatalytic activity towards degradation of tetracycline. *Mater. Res. Bull.* 135. <https://doi.org/10.1016/j.materresbull.2020.111161>.
- Xue, W.J., Peng, Z.W., Huang, D.L., Zeng, G.M., Wen, X.J., Deng, R., Yang, Y., Yan, X.L., 2019. In situ synthesis of visible-light-driven Z-scheme $\text{AgI}/\text{Bi}_2\text{WO}_6$ heterojunction photocatalysts with enhanced photocatalytic activity. *Ceram. Int.* 45, 6340–6349. <https://doi.org/10.1016/j.ceramint.2018.12.119>.
- Yang, Z.F., Shao, L.H., Wang, L.L., Xia, X.N., Liu, Y.T., Cheng, S., Yang, C., Li, S.J., 2020. Boosted photogenerated carriers separation in Z-scheme $\text{Cu}_3\text{P}/\text{ZnIn}_2\text{S}_4$ heterojunction photocatalyst for highly efficient H_2 evolution under visible light-ScienceDirect. *Int. J. Hydrogen Energy* 45, 14334–14346. <https://doi.org/10.1016/j.ijhydene.2020.03.139>.
- Yuan, D.L., Sun, M.T., Tang, S.F., Zhang, Y.T., Wang, Z.T., Qi, J.B., Rao, Y.D., Zhang, Q.R., 2020. All-solid-state $\text{BiVO}_4/\text{ZnIn}_2\text{S}_4$ Z-scheme composite with efficient charge separations for improved visible light photocatalytic organics degradation. *Chin. Chem. Lett.* 31 (2), 547–550. <https://doi.org/10.1016/j.ccllet.2019.09.051>.
- Zhang, B.B., Chou, L.J., Bi, Y.P., 2020a. Tuning surface electronegativity of BiVO_4 photoanodes toward high-performance water splitting. *Appl. Catal. B-Environ.* 162. <https://doi.org/10.1016/j.apcatb.2019.118267>.
- Zhang, L.Y., Dai, Z.X., Zheng, G.H., Yao, Z.F., Mu, J.J., 2018. Superior visible light photocatalytic performance of reticular BiVO_4 synthesized via a modified sol-gel method. *RSC Adv.* 8, 10654–10664. <https://doi.org/10.1039/C8RA00554K>.
- Zhang, N., Liu, T., Zhao, F., Zhang, X.C., Wang, Y.H., 2021a. The band engineering of 2D-hybridized $\text{PCN-Sb}_2\text{MoO}_6\text{-Bi}_2\text{O}_3$ nanomaterials with dual Z-scheme heterojunction for enhanced photocatalytic water splitting without sacrificial agents. *Sustain. Energ. Fuels* 5, 2325–2334. <https://doi.org/10.1039/D1SE00290B>.
- Zhang, J.L., Ma, Z., 2017. $\text{AgI}/\beta\text{-Ag}_2\text{MoO}_4$ heterojunctions with enhanced visible-light-driven catalytic activity. *J. Taiwan Inst. Chem. E* 81, 225–231. <https://doi.org/10.1016/j.jtice.2017.10.018>.
- Zhang, J.L., Ma, Z., 2018b. $\text{Ag}_3\text{VO}_4/\text{AgI}$ composites for photocatalytic degradation of dyes and tetracycline hydrochloride under visible light. *Mater. Lett.* 216, 216–218. <https://doi.org/10.1016/j.matlet.2018.01.035>.
- Zhang, W.Q., Shi, W.L., Sun, H.R., Shi, Y.X., Luo, H., Jing, S.R., Fan, Y.Q., Guo, F., Lu, C.Y., 2021b. Fabrication of ternary $\text{CoO}/\text{g-C}_3\text{N}_4/\text{Co}_3\text{O}_4$ nanocomposite with p-n-p type heterojunction for boosted visible-light. *J. Chem. Technol. Biotechnol.* 96, 1854–1863. <https://doi.org/10.1002/jctb.6703>.
- Zhang, M., Yao, J.C., Arif, M., Bo, Q., Yin, H.F., Liu, X.H., Chen, S. M., 2020c. 0D/2D $\text{CeO}_2/\text{ZnIn}_2\text{S}_4$ Z-scheme heterojunction for visible-light-driven photocatalytic H_2 evolution. *Appl. Surf. Sci.* 526. <https://doi.org/10.1016/j.apsusc.2020.145749>.
- Zhang, J.J., Zhu, Z.R., Jiang, J.C., Li, H., 2020b. Fabrication of a novel $\text{AgI}/\text{LaFeO}_3/\text{g-C}_3\text{N}_4$ dual Z-scheme photocatalyst with enhanced photocatalytic performance. *Mater. Lett.* 262. <https://doi.org/10.1016/j.matlet.2019.127029>.
- Zhao, Z.W., Li, X.F., Dai, K., Zhang, J.F., Dawson, G., 2022. In-situ fabrication of $\text{Bi}_2\text{S}_3/\text{BiVO}_4/\text{Mn}_0.5\text{Cd}_0.5$ S-DETA ternary S-scheme heterostructure with effective interface charge separation and CO_2 reduction performance. *J. Mater. Sci. Technol.* 117, 109–119. <https://doi.org/10.1016/j.jmst.2021.11.046>.
- Zhou, L.P., Dai, S.Q., Xu, S., She, Y.Q., Li, Y.L., Leveneur, S., Qin, Y.L., 2021. Piezoelectric effect synergistically enhances the performance of $\text{Ti}_{32}\text{-oxo-cluster}/\text{BaTiO}_3/\text{CuS}$ p-n heterojunction photocatalytic degradation of pollutants. *Appl. Catal. B-Environ.* 291. <https://doi.org/10.1016/j.apcatb.2021.120019>.
- Zhou, Q., Song, Y., Li, N.J., Chen, D.Y., Xu, Q.F., Li, H., He, J.H., Lu, J.M., 2020. Direct dual Z-scheme $\text{Bi}_2\text{WO}_6/\text{GQDs}/\text{WO}_3$ inverse opals for enhanced photocatalytic activities under visible light. *ACS Sustain. Chem. Eng.* 8, 7921–7927. <https://doi.org/10.1021/acssuschemeng.0c01548>.
- Zhu, Z., Hong, W.G., Chen, C.Y., Wu, R., 2020. Novel nanoarchitectonics olive-Like Pd/BiVO_4 for the degradation of gaseous formaldehyde under visible light irradiation. *J. Nanosci. Nanotechnol.* 20, 2689–2697. <https://doi.org/10.1166/jnn.2020.17430>.